Mathematical Modelling of Residual Stresses in End Milling

Ojolo, S.J., Ogundare, A.A., Kofoworola, O.
Mechanical Engineering Department, University of Lagos, Nigeria
Email: sojolo@unilag.edu.ng

Abstract
During end milling, the residual stresses is developed from two sources which includes, stresses due to plastic deformation of material and then stresses due to thermal energy generated. This work looks into the two sources combined into one and then predicts how to best combine the machining parameters in order to minimize the residual stresses in the components. The aim of this work is to develop a mathematical model that can be used to predict the residual stresses in milling. Analytical method was used in developing this model; the model captured the mechanical stress and the thermal stress. The simulation was done with MATLAB and from the results obtained; it was observed that mill cutter with nose radius of 0.4mm and a constant cutting speed of 3m/min while the depth of cut varies from 0.1mm to 0.4mm, the resulting residual stress varied from 50MPa to 150MPa respectively. From the graphs it was also observed that the value of the residual stress at a particular depth of cut is the same in both the x-x and z-z directions and that the stress reduces exponentially as it approaches zero.

Keywords: End milling, Residual Stresses, Simulation, Stainless Steel

1.0 INTRODUCTION

Residual stress exists in a body after all the external loads are removed. Manufacturing processes are the most common causes of the residual stress. The effects of residual stress could be both positive and detrimental on the deformation behavior, fatigue life, dynamic strength, chemical resistance and magnetic properties of machined component (Wu and Matsumoto, 1990) such as the turbine engine fan blades. Laser peening imparts deep beneficial compressive residual stresses into metal components and it is used in toughened glass to allow for large, thin, crack and scratch-resistant as found in glass displays on smart phones. In machining, the sources of residual stress include plastic deformation of the material and high thermal gradients in the cutting zone. These two sources are complex and do affect each other. Plastic deformation occurs during chip formation when the material is being sheared in the cutting zone. Residual stresses play an important role in the performance of machined Components. The functional behavior of machined components can be enhanced or impaired by residual stresses (Su, 2006).

Thus, the residual stress imparted by machining is an important aspect of research on machining and overall part quality. The residual stresses induced by turning are tensile at the surface and compressive as machining depth increase, while the milling operation with induces more compressive residual stresses (Wang *et. al*, 2017). Residual stress is measured by either destructive or non-destructive method. A typical example of the non-destructive method is the X-ray diffraction, while the destructive method which are all based on the principle of stress relaxation includes hole drilling and ring coring, deep hole drilling, and the slit milling method (Mansilla *et. al*, 2015).

2.0 THERMO-MECHANICAL MODELING OF STRESSES

Analytical method of modelling is used in this work. This is because it gives the most accurate value in the prediction of the residual stress.

2.1 Cutting Force Model

The stresses generated in the work piece during cutting are due to traction in the shear zone and traction due to the rubbing of the tool edge on the surface of the work piece.

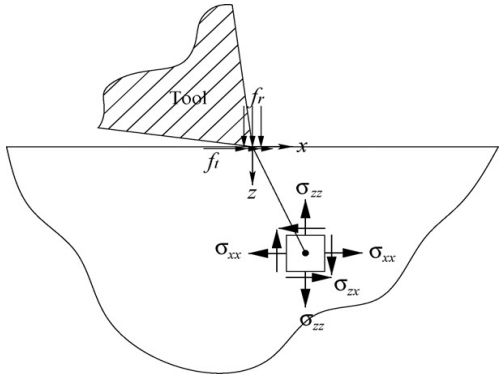

Figure 1: Orthogonal cutting cutting operation model

From Figure 1, the differential tangential dF_t, radial dF_r and axial dF_a cutting forces acting on infinitesimal cutting edge segment form the governing equations, which are:

$$dF_t(i,j,k) = K_t A_c(i,j,k) = K_t t_c(i,j,k)dz \quad (1)$$

$$dF_r = K_r dF_t(i,j,k) = K_r K_t t_c(i,j,\mathrm{k})\,\mathrm{dz} \quad (2)$$

$$dF_a = K_a dF_t(i,j,k) = K_a K_t t_c(i,j,k)dz \quad (3)$$

The axial force, dF_a acts on the elemental disk along with the tangential force and radial forces. This force is present since, in the general case, the helix angle of the end mill is non-zero, thus producing an oblique cutting geometry. The axial force, however, is typically much smaller than either the tangential or radial forces, and in addition does not contribute greatly to the bending moment produced on the cutter. Thus, the axial force may be neglected.

$$dF_t(i,j,k) = K_t A_c(i,j,k) = K_C t_c(i,j,k)dz \quad (4)$$

Where, $t_c = f_t \operatorname{Sin}\beta(i,j,k) f_t = V_f / N_s N_f$

$$dF_t = K_t f_t Sin\beta(i,j,k)dz \quad (5)$$

So, $$dF_t = \frac{K_t V_f}{N_s V_f} Sin\beta(i,j,k)dz \quad (6)$$

Similarly, $$dF_r = \frac{K_r K_t V_f}{N_s V_f} Sin\beta(i,j,k)dz \quad (7)$$

But, $\beta(i,j,k) = -\theta(j) + (K-1)\gamma_f - \gamma_{hx}$ and $\gamma_{hx} = z(t)\tan\alpha_{ht}/RAD$

Thus, $$\beta(i,j,k) = \frac{z(t)\tan\alpha_{hx}}{RAD} + (K-1)\gamma_f - \theta(j) \quad (8)$$

So that, $$dF_t = \frac{K_t V_f}{N_s N_f} Sin\left[\frac{z(i)\tan\alpha_{hx}}{RAD} + (K-1)\gamma_f - \theta(j)\right]dz \quad (9)$$

Likewise, $$dF_r = \frac{K_r K_t V_f}{N_s N_f} Sin\left[\frac{z(i)\tan\alpha_{hx}}{RAD} + (K-1)\gamma_f - \theta(j)\right]dz \quad (10)$$

On integration and further simplification of the trigonometric factors,

$$F_t = \frac{2K_t V_f}{N_s N_f}\left(\frac{RAD}{\tan\alpha_{hx}}\right)\left[Sin\left[\begin{bmatrix}\frac{z_u(i)+z_l(i)\tan\alpha_{hx}}{RAD}\\ +(K-1)\gamma_f-\theta(j)\end{bmatrix}\right] Sin\frac{\left(z_u(i)-z_l(i)\tan\alpha_{hx}\right)}{RAD}\right]dy \quad (11)$$

$$F_r = \frac{2K_r K_t V_f}{N_s N_f}\left(\frac{RAD}{\tan\alpha_{hx}}\right)\left[\begin{bmatrix} Sin\left[\frac{z_u(i)+z_l(i)\tan\alpha_{hx}}{2RAD}\right]\\ +(K-1)\gamma_f-\theta(j) Sin\left[\frac{\left(z_u(i)-z_l(i)\tan\alpha_{hx}\right)}{2RAD}\right]\end{bmatrix}\right] \quad (12)$$

Where, $dF_t(i,j,k)$ is the elemental tangential force, $dF_r(i,j,k)$ is the elemental radial force, $A_c(i,j,k)$ and $t_c(i,j,k)dz$ is the contact area or chip load, $t_c(i,j,k)$ is the uncut chip thickness, and K_t and K_r are the empirically determined function. α_{hx} is the helix angle of the end mill. Given the existence of cutter run out, it has been shown (Kline et al., 1982; Sutherland and Devor, 1986) that the chip thickness may be expressed as

$$t_c(i,j,k) = Min\left[mf_t Sin\beta(i,j,k) + R(i,\mathrm{k},\mathrm{m})\right]$$

$$R(i,j,k) = \left[\begin{bmatrix} RAD^2+\rho^2+2RAD\rho\cos\left[\lambda-\left(K-1\right)\gamma_f-\gamma hx\right]\\ +\left(L-Z\right)^2 Sin\tau\left[\rho\cos\phi+RAD\cos\left(\lambda-\left(K-1\right)\right)\gamma_f\right]\end{bmatrix}\right]^{\frac{1}{2}} \quad (13)$$

ρ and λ are parameters which describe the parallel axis offset. τ and ϕ are parameters which describe the cutter tilt geometry. Z is the distance from the fixed end of the cutter to the axial position of interest, and m is an index used to consider proceeding flutes.

However, in end milling process, both primary and regenerative feedbacks are present. With the incorporation of both the primary and the regenerative feedback effects, the chip thickness may be expressed as

$$t_c\left(i,j,k\right) = Min\left[\begin{bmatrix} mf_t Sin\beta\left(i,\mathrm{j},\mathrm{k}\right)+R\left(i,k\right)-R\left(i,k-m\right)\\ +\left[x\left(i,j\right)-x\left(i,n\right)\right]Sin\beta\left(i,j,k\right)\\ -\left[y\left(i,j\right)-y(i,j)\cos\beta\left(i.j.k\right)\right]\end{bmatrix}\right] \quad (14)$$

$x(i,j)$ is the relative displacement in the x-direction of the axial disk at the angular position of the end mill from the work piece, and $y(i,j)$ is the displacement in the y-direction,

$$n = \frac{j-\left(k-m\right)\gamma_{ff}}{d\theta} \quad (15)$$

2.2 Mechanical Stress Model

Considering the mechanical loading due to the cutting forces, assuming a state of plane strain in y-direction$\left(\varepsilon_{yy}=0\right)$, stresses under the normal compressive pressure radial force, F_r and tangential traction, F_t as given with the associated coordinate system are estimated using contact mechanics

$$\sigma_{xx}^{mech} = \frac{-2z}{\pi}\int_{-a}^{a}\frac{F_r\left(x-s\right)^2}{\left[\left(x-s\right)^2+z^2\right]^2}ds - \frac{2}{\pi}\int_{-a}^{a}\frac{F_t\left(x-s\right)^3}{\left[\left(x-s\right)^2+z^2\right]^2}ds \quad (16)$$

$$\sigma_{zz}^{mech} = \frac{-2z^3}{\pi}\int_{-a}^{a}\frac{F_r}{\left[\left(x-s\right)^2+z^2\right]^2}ds - \frac{2z^2}{\pi}\int_{-a}^{a}\frac{F_t\left(x-s\right)}{\left[\left(x-s\right)^2+z^2\right]^2}ds \quad (17)$$

$$\sigma_{xz}^{mech} = \frac{-2z^2}{\pi}\int_{-a}^{a}\frac{F_r\left(x-s\right)}{\left[\left(x-s\right)^2+z^2\right]^2}ds - \frac{2z}{\pi}\int_{-a}^{a}\frac{F_t\left(x-s\right)^2}{\left[\left(x-s\right)^2+z^2\right]^2}ds \quad (18)$$

On integrating the above with the limit of the integrals [-a, a] as a function of the cutting edge radius, we get

$$\sigma_{xx}^{mech} = \frac{F_t}{\pi}\left[\ln\left(a^2-2as+s^s+z^2\right)-\ln\left(a^2+2as+s^2+z^2\right)\right]$$
$$-\frac{F_r}{\pi}\left[\arctan\left(\frac{a-s}{z}\right)-\arctan\left(\frac{a+s}{z}\right)\right]+\frac{2az\left(a^2F_r-s^2F_r+2szF_t+z^2F_r\right)}{\pi\left(a^2-2as+s^s+z^2\right)\left(a^2+2as+s^2+z^2\right)} \quad (19)$$

$$\sigma_{zz}^{mech} = -\frac{2z^3F_r}{\pi}\left[\begin{array}{l}\dfrac{2(a-s)}{4\left[z^2\left(a^2-2as+s^2+z^2\right)\right]}+\left(\dfrac{1}{2\left(z^2\sqrt{z^2}\right)}\times\arctan\left[\dfrac{2(a-s)}{2\sqrt{z^2}}\right]\right)\\ +\dfrac{2(a+s)}{4\left[z^2\left(a^2+2as+s^2+z^2\right)\right]}+\left(\dfrac{1}{2\left(z^2\sqrt{z^2}\right)}\times\arctan\left[\dfrac{2(a+s)}{2\sqrt{z^2}}\right]\right)\end{array}\right] \quad (20)$$
$$+\frac{2z^2F_t}{\pi}\left[\frac{1}{2\left(a^2-2as+s^2+z^2\right)}-\frac{1}{2\left(a^2+2as+s^2+z^2\right)}\right]$$

$$\sigma_{xz}^{mech} = \frac{2z^2F_r}{\pi}\left[\frac{1}{2\left(a^2-2as+s^2+z^2\right)}-\frac{1}{2\left(a^2+2as+s^2+z^2\right)}\right]$$
$$+\frac{2zF_t}{\pi}\left[\begin{array}{l}\dfrac{a}{2\left(a^2-2as+s^2+z^2\right)}-\dfrac{s}{2\left(a^2-2as+s^2+z^2\right)}-\left(\dfrac{1}{2\sqrt{z^2}}\times\arctan\left[\dfrac{2(a-s)}{2\sqrt{z^2}}\right]\right)\\ +\dfrac{a}{2\left(a^2+2as+s^2+z^2\right)}+\dfrac{s}{2\left(a^2+2as+s^2+z^2\right)}+\left(\dfrac{1}{2\sqrt{z^2}}\times\arctan\left[\dfrac{2(a+s)}{2\sqrt{z^2}}\right]\right)\end{array}\right] \quad (21)$$

2.3 Thermal Stresses

Modelling the internal heat generation in the work piece is

$$Q_g = Q_f + Q_s \quad (22)$$

Q_f is the friction heat generation and Q_s is the shear or plastic deformation heat generation

$$Q_f = F_fV_c = \frac{\tau hV\sin\beta_n}{\cos\left(\varphi_n+\beta_n-\alpha_n\right)\sin\left(\varphi_n-\alpha_n\right)} \quad \text{and} \quad Q_s = F_sV_c = \frac{\tau hV\cos\alpha_n}{\sin\alpha_n\cos\left(\varphi_n-\alpha_n\right)}$$

$$Q_g = \tau hV\left[\frac{\sin\beta_n \sin\alpha_n \cos(\varphi_n - \alpha_n) + \cos\alpha_n \cos\left(\varphi_n + \beta_n - \alpha_n\right)\sin\left(\varphi_n - \alpha_n\right)}{\sin\alpha_n \sin\left(\varphi_n - \alpha_n\right)\cos\left(\varphi_n - \alpha_n\right)\cos\left(\varphi_n + \beta_n - \alpha_n\right)}\right] \quad (23)$$

Replacing the terms in parenthesis with η, Q_g becomes

$$Q_g = \eta\tau hV \quad (24)$$

The resulting thermal stress components from the thermal stresses developed by [7] are

$$\sigma_{xx}^{ther} = \frac{-\alpha E}{1-2\nu}\int_0^{\infty}\int_{-\infty}^{\infty}\left[G_{xh}\frac{\partial T}{\partial x}\left(x^1, z^1\right) + G_{xv}\frac{\partial T}{\partial x}\left(x^1, z^1\right)\right]dx^1 dz^1$$
$$+\frac{2z}{\pi}\int_{-\infty}^{\infty}\left[\frac{\rho(t)\left(t-x\right)^2}{\left[\left(t-x\right)^2 + z^2\right]^2}dt\right] - \frac{\alpha ET\left(x,z\right)}{1-2\nu} \quad (25)$$

$$\sigma_{zz}^{ther} = \frac{-\alpha E}{1-2\nu}\int_0^{\infty}\int_{-\infty}^{\infty}\left[G_{zh}\frac{\partial T}{\partial x}\left(x^1, z^1\right) + G_{zv}\frac{\partial T}{\partial x}\left(x^1, z^1\right)\right]dx^1 dz^1$$
$$+\frac{2z^3}{\pi}\int_{-\infty}^{\infty}\left[\frac{\mathrm{p}(t)}{\left[\left(t-x\right)^2 + z^2\right]^2}dt\right] - \frac{\alpha ET\left(x,z\right)}{1-2\nu} \quad (26)$$

$$\sigma_{xz}^{ther} = \frac{-\alpha E}{1-2\nu}\int_0^{\infty}\int_{-\infty}^{\infty}\left[G_{xzh}\frac{\partial T}{\partial x}\left(x^1, z^1\right) + G_{xzv}\frac{\partial T}{\partial x}\left(x^1, z^1\right)\right]dx^1 dz^1 + \frac{2z^2}{\pi}\int_{-\infty}^{\infty}\left[\frac{\mathrm{p}(t)\left(x-t\right)}{\left[\left(t-x\right)^2 + z^2\right]^2}dt\right] \quad (27)$$

Where, $p\left(t\right) = \dfrac{\varepsilon ET\left(x,z\right)}{1-2\nu}$

For a two dimensional temperature distribution;

$$T\left(x,z,t\right) = \frac{Q}{\left(4\pi\alpha t\right)^{\frac{3}{2}}}e^{-\frac{x^2+z^2}{4\alpha t}} \quad (28)$$

$$\frac{dT}{dx} = -\frac{Qx}{2\alpha t\left(4\pi\alpha t\right)^{\frac{3}{2}}}e^{-\frac{x^2+z^2}{4\alpha t}} \quad (29)$$

$$\frac{dT}{dz} = \frac{Qx}{2\alpha t\left(4\pi\alpha t\right)^{\frac{3}{2}}}e^{-\frac{x^2+z^2}{4\alpha t}} \quad (30)$$

Considering heat sources at points r_1 and r_2. The Green's function for this space of thermal conductivity, k is

$$G\left(x,h\right) = G_{xxh} = G\left(X, X^{'}\right) = \frac{1}{4\pi k}\left[\frac{1}{r_1} - \frac{1}{r_2}\right] \quad (31)$$

Where $r_1 = \sqrt{\left(x-x^{'}\right)^2 + \left(z-z^{'}\right)^2}$ and $r_2 = \sqrt{\left(x+x^{'}\right)^2 + \left(z+z^{'}\right)^2}$

$$G(x,h) = G_{xxh} = G\left(X, X^{'}\right) = \frac{1}{4\pi k}\left[\frac{1}{\sqrt{\left(x-x^{'}\right)^2+\left(z-z^{'}\right)^2}} - \frac{1}{\sqrt{\left(x+x^{'}\right)^2+\left(z+z^{'}\right)^2}}\right] \quad (32)$$

Therefore, the value of the thermal stress in the $x-x$ and $z-z$ direction are as follows

$$\sigma_{xx}^{therm} = K_{therm}\int_0^{\infty}\int_{-\infty}^{\infty}\left[\frac{1}{\sqrt{\left(x-x^{'}\right)^2+\left(z-z^{'}\right)^2}} - \frac{1}{\sqrt{\left(x+x^{'}\right)^2+\left(z+z^{'}\right)^2}}\right]dx^{'}dz^{'} \quad (33)$$

$$+\frac{2z}{\pi}\int_{-\infty}^{\infty}\frac{p(t)(t-x)^2}{\left[(t-x)^2+z^2\right]^2}dt - \frac{\alpha ET(X.Y)}{1-2\nu}$$

$$\sigma_{xx}^{therm} = \frac{K_{therm}}{4\pi k}\int_0^{\infty}\int_{-\infty}^{\infty}\left[\frac{1}{\sqrt{\left(x-x^{'}\right)^2+\left(z-z^{'}\right)^2}} - \frac{1}{\sqrt{\left(x+x^{'}\right)^2+\left(z+z^{'}\right)^2}}\right]dx^{'}dz^{'} \quad (34)$$

$$+\frac{2z}{\pi}\int_{-\infty}^{\infty}\frac{p(t)(t-x)^2}{\left[(t-x)^2+z^2\right]^2}dt - \frac{\alpha ET(X.Y)}{1-2\nu}$$

Where, $K_{therm} = -\frac{EQx}{4\pi kt(1-2\upsilon)(4\pi\alpha t)^{\frac{3}{2}}}e^{-\frac{x^2+z^2}{4\alpha t}}(x^{'},z^{'})$

2.4 Residual Stress Model

The resultant residual stress is the addition of the mechanical stress and thermal stress in the various directions respectively. Therefore, residual stresses are given as

$$\sigma_{xx}^{r} = \sigma_{xx}^{mech} + \sigma_{xx}^{therm} \quad (35)$$

$$\sigma_{zz}^{r} = \sigma_{zz}^{mech} + \sigma_{zz}^{therm} \quad (36)$$

$$\sigma_{xz}^{r} = \sigma_{xz}^{mech} + \sigma_{xz}^{therm} \quad (37)$$

3.0 SIMULATION AND DISCUSSION

The results of the simulation of the residual stress for the developed model are shown below. The predicted residual stress follows the same trend as the depth of cut varied in the modelling of residual stresses (Ulutan *et. al*, 2007). The residual stress is a function of depth of cut when nose radius is kept constant. The simulation was done using a nose radius of 0.4mm with depth of cut ranging from 1mm to 4mm.

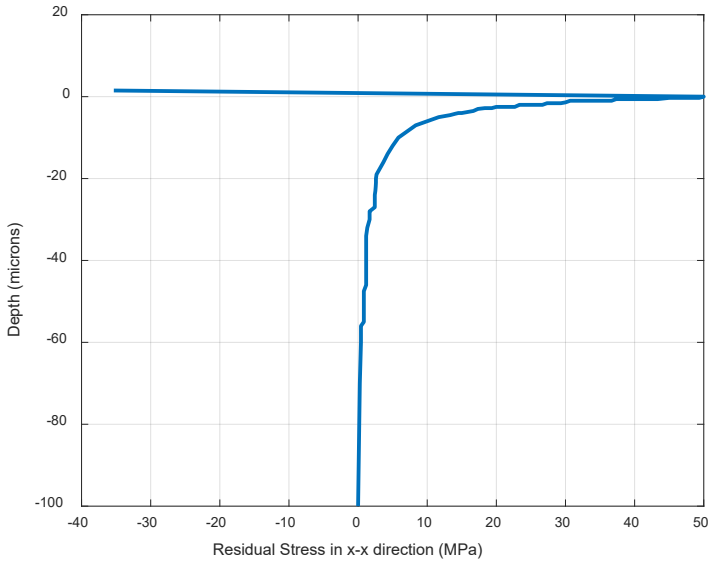

Figure 2: ***A plot of the depth beneath the surface of the work piece against the residual stress in x-x direction at a depth of cut of 1mm***

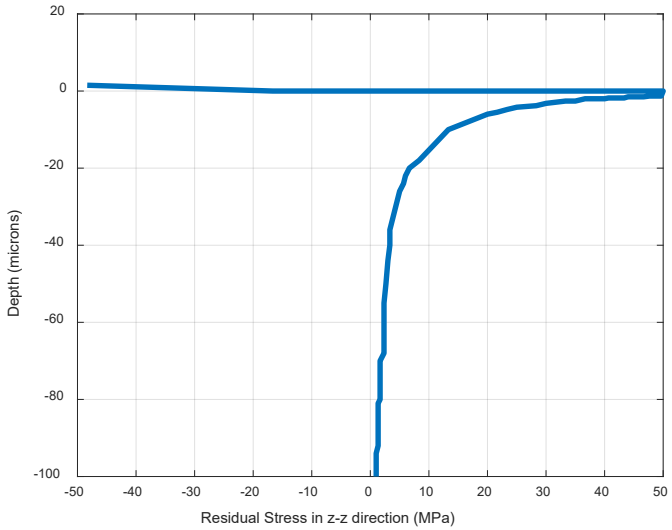

Figure 3: ***A plot of depth into the work material against residual stress in the z-z direction at a depth of cut of 1mm***

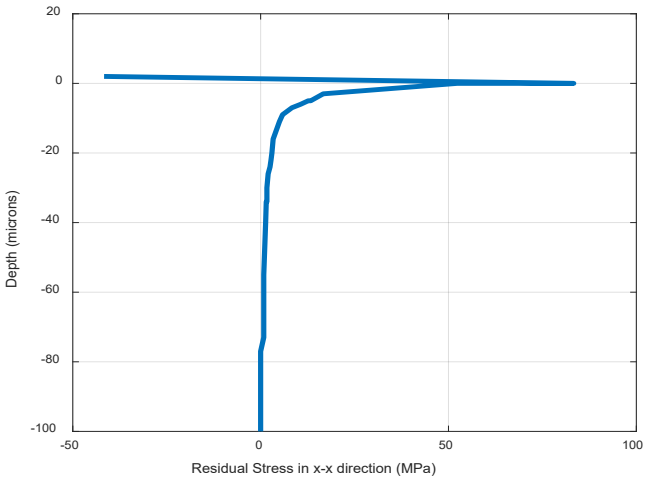

Figure 4: ***A plot of depth into the work material against residual stress in the x-x direction at a depth of cut of 2mm***

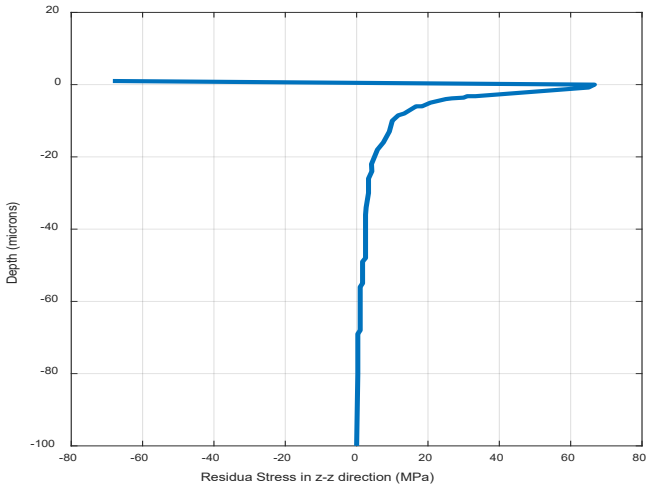

Figure 5: ***A plot of depth into the work material against residual stress in the z-z direction at a depth of cut of 2mm***

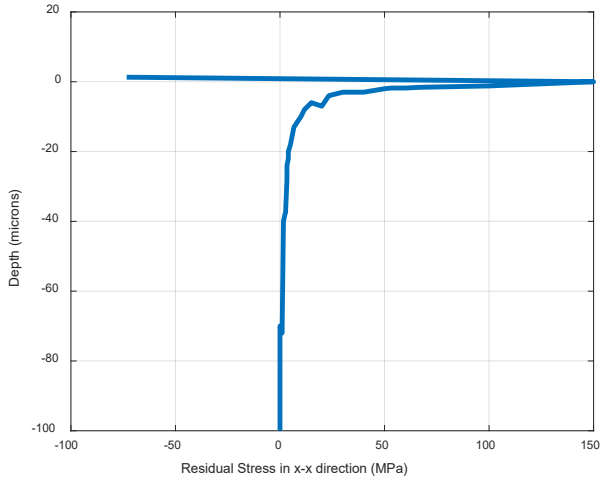

Figure 6: ***A plot of depth into the work material against residual stress in the x-x direction at a depth of cut of 4mm***

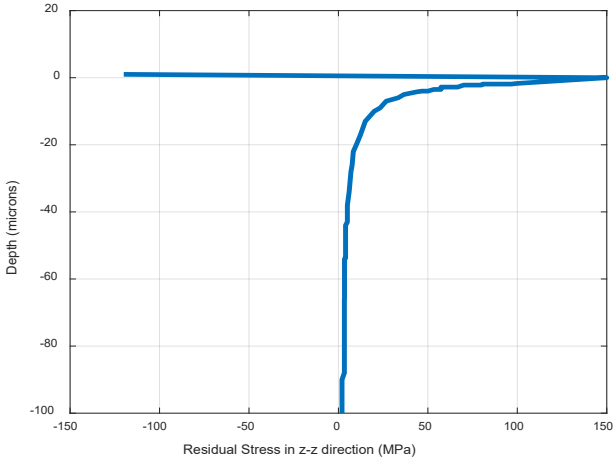

Figure 7: ***A plot of depth into the work material against residual stress in the z-z direction at a depth of cut of 4mm***

Figure 2 shows the residual stress in the $x-x$ direction at a depth of 1mm beneath the surface of the work piece. The maximum residual stress is 50 MPa at the surface of the material and reduces exponentially towards zero as the depth increased. This can be attributed to mechanical stresses due to the effect of edge radius between the tool and the work piece and the thermal

stress. The thermal stress decreases exponentially as the moving tool creates a moving heat source which determines the temperature rise due to rubbing between the cutting edge and the work piece and is highest at the point of contact with the work piece. Also, the residual stress becomes negligible at a depth of more than 80 microns beneath the surface of the material which agrees with (Liu *et. al*, 2004) in which a maximum stress of about 110 MPa and residual stress becoming negligible at a depth of 90 microns beneath the surface of the work piece.

Figure 3 shows the residual stress value at a depth of 1mm, and nose radius of 0.4mm in $z-z$ direction, it shows that residual stress are significant at the surface, this is as a result of the combination of the mechanical stress and thermal stress which emerges from the cutting force action, which also is in agreement with (Okushima and Kakino, 1972). The stress attains a minimum value at a depth of 100microns beneath the surface of the material. It reduces exponentially beneath the work piece, this is because during orthogonal cutting operation, the maximum work piece temperature occurs at the surface near the tool tip, and the temperature drops quickly behind the tool tip.

Form Figure 4 the maximum residual stress increased to 85 MPa at the surface of the material, because the Cauchy stress tensor increased and becomes negligible at a depth of more than 60 microns beneath the surface of the material, this is because a larger shear angle is produced which alters the penetration depth. This agrees favourably with the work of (Ulutan *et al*., 2017).

In Figure 5 the maximum residual stress of 70 MPa was obtained at the surface of the material and reduces exponentially towards zero with the depth beneath the material. It is observed that the residual stress becomes negligible at a depth of close to 100 microns beneath the surface of the material. This can be compared reasonably with Figure 3 where a maximum stress of about 50 MPa is reached and approaches a minimum value at a depth close to 100microns beneath the surface of the work piece

Figure 6 shows a plot of the depth beneath the surface of the work piece against the residual stress in $x-x$ direction at a depth of cut of 4mm and nose radius of 0.4 mm. The maximum residual stress is 150 MPa at the surface of the material. This agrees with the effect of temperature on residual stresses being more prominent at the surface as predicted by (Su, 2006). It reduces exponentially towards zero with the depth beneath the material. It is observed that the residual stress becomes negligible at a depth of more than 60 microns beneath the surface of the material, this agrees with (Ulutan *et al*., 2017) who discovered that the residual approaches zero with various nose radius value and depth of cut values. Figure 7 which shows a plot of the depth beneath the surface of the work piece against the residual stress in $x-x$ direction at a depth of cut of 4mm and nose radius of 0.4 mm result follows similar assertions from the previous graphs and discussions

4.0 CONCLUSION

The mathematical model showed how the residual stresses varied from 50MPa to 150MPa at values of depth of cut varying from 1mm to 4mm. It was shown that the residual stress has the same profile for all values of the depth of cut. The method was able to accurately predict the stress profile beneath the surface of the work piece. This clearly showed that there is an exponential reduction of the stress as it approaches zero beneath the surface of the work piece. The model was able to capture the residual stress by capturing the forces involved while taking into consideration the forces due to temperature variation. The model allows the prediction of

residual stresses with acceptable accuracy. With specified cutting parameters, the model can be used to predict the residual stress in milling operations.

REFERENCES

Kline, W. A., Devor, R. E., and Lindberg, J. R., (1982). The prediction of cutting forces in end milling with application to cornering cuts. International Journal of Machine Tool Design and Research, 22(1): 7-22.

Liu, M., Takagi, J. I. and Tsukuda, A. (2004). Effect of Tool Nose Radius and Tool Wear on Residual Stress Distribution in Hard Turning of Bearing Steel. Journal of Materials Processing Technology, 150(3): 234-241

Mansilla, C., Martinez-Martinez, D., Ocelik, V., and De Hosson, J. T. M. (2015). On the determination of local residual stress gradients by the slit milling method. Journal of Materials Science, 50(10): 3646-3655.

Okushima, K., and Kakino, Y. (1972). Study of the residual stress produced by metal cutting, Mem. Fac. Eng. Kyoto Univ., April, 34(2): 234-248.

Su, J.C., (2006). Residual stress modeling in machining processes, Georgia Institute of Technology: Atlanta.

Sutherland, J. W., and Devor, R., (1986). An improved method for cutting force and surface error prediction in flexible end milling systems. Journal of engineering for industry, 108(4): 269-279.

Ulutan, D., Alaca, B. E., and Lazoglu, I. (2007). Analytical modeling of residual stresses in machining. Journal of Materials Processing Technology, 183(1):77-87.

Wang, J., Zhanga, D., Wua, B., Luo, M. (2017). Residual Stresses Analysis in Ball end Milling of Nickel-Based Superalloy Inconel 718, Materials Research. 20(6): 1681-1689

Wu, D.W. and Matsumoto, Y. (1990). Effect of hardness on residual stresses in orthogonal machining of ANSI 4340 steel. Journal of Engineering for Industry, 112(3): 245-252.